

Synthesis of Homogeneous Manganese-Doped Titanium Oxide Nanotubes from Titanate Precursors

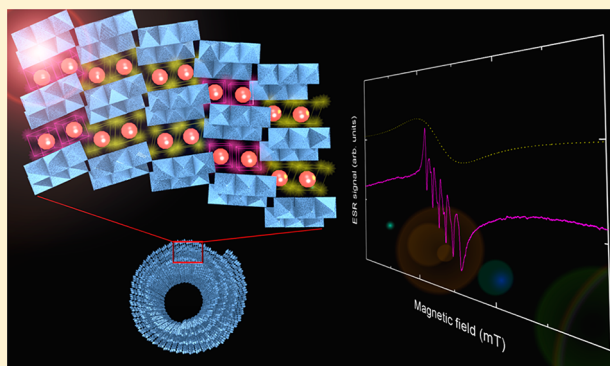
Péter Szirmai,[§] Endre Horváth,[†] Bálint Náfrádi,[†] Zlatko Micković,[†] Rita Smajda,[†] Dejan M. Djokić,[†] Kurt Schenk,[‡] László Forró,[†] and Arnaud Magrez^{*,†}

[†]Laboratory of Physics of Complex Matter, Ecole Polytechnique Fédérale de Lausanne, 1015 Lausanne, Switzerland

[‡]Institute of Physics of Biological Systems, Ecole Polytechnique Fédérale de Lausanne, 1015 Lausanne, Switzerland

[§]Department of Physics, Budapest University of Technology and Economics, PO Box 91, Budapest H-1521, Hungary

ABSTRACT: We report a novel synthesis route of homogeneously manganese-doped TiO₂ nanotubes in a broad concentration range. The scroll-type trititanate (H₂Ti₃O₇) nanotubes prepared by hydrothermal synthesis were used as precursors. Mn²⁺ ions were introduced by an ion exchange method resulting Mn_xH_{2-x}Ti₃O₇. In a subsequent heat treatment, they were transformed into Mn_yTi_{1-y}O₂, where $y = x/(3 + x)$. The state and the local environment of the Mn²⁺ ions in the precursor and final products were studied by the electron spin resonance (ESR) technique. It was found that the Mn²⁺ ions occupy two positions: the first having an almost perfect cubic symmetry while the other is in a strongly distorted octahedral site. The ratio of the two Mn²⁺ sites is independent of the doping level and amounts to 15:85 in Mn_xH_{2-x}Ti₃O₇ and to 5:95 in Mn_yTi_{1-y}O₂. SQUID magnetometry does not show long-range magnetic order in the homogeneously Mn²⁺-doped nanotubes.



INTRODUCTION

Titanium dioxide has been extensively studied due to its high thermal and chemical stability, abundance, and environmental friendliness. This material is widely used in heterogeneous catalysis and photocatalysis, as white pigment in paints, food and cosmetic products, corrosion-protective coatings, and biocompatible layer of bone implants.¹ Nanostructured TiO₂ films are used as photoanode in solar-to-electric energy conversion devices such as dye-sensitized solar cells² (DSSCs), in gas sensors,³ and in supercapacitors.⁴ It is expected that a detailed study of the structural and electronic properties of TiO₂ will help in the understanding of the material's behavior as well as to improve the performances of the previously mentioned applications.^{5,6}

Recently, TiO₂ nanotubes and nanowires have received a great deal of attention. These elongated structures possess large surface area and can be used to prepare novel 3D and highly crystalline structures exhibiting large porosity from which efficient DSSCs are built.⁷ Titanate nanowires can serve as a scaffold for self-organization of organic molecules. Based on this property, high sensitivity optical humidity sensors with fast response time have been realized.⁸ Furthermore, TiO₂ is a popular material in spintronics.⁹ It is expected to show room temperature ferromagnetism when doped with transition metal ions.^{10,11} TiO₂ thin films have shown this effect above 5% Mn substitutional doping.^{12,13} A similar phenomenon has been observed at low doping level in bulk manganese-doped TiO₂ produced by sintering.¹⁴ Ferromagnetism is explained on the

basis of the bound magnetic polaron model. However, these results are the subject of controversy as ferromagnetism could arise from impurities, aggregation of doping or magnetic clusters.¹⁵ These flaws could be the product of inhomogeneously prepared TiO₂ precursors or the result of segregation caused by the high-temperature synthesis process.¹⁶ This ambiguity underscores the need to elaborate a reliable synthesis method for homogeneous doping of TiO₂ with transition metal ions.

Here we report a low-temperature synthesis route of homogeneously doped TiO₂ nanotubes (NTs) with Mn²⁺ ions using scroll-type trititanate (Na₂Ti₃O₇) nanotube precursor (Na-NTs) produced by an alkali hydrothermal treatment of TiO₂. These multiwalled nanotubes are composed of stepped or corrugated host layers of edge-sharing TiO₆ octahedrons having interlayer alkali metal cations. By ionic exchange, the alkali titanates can be easily modified into Mn_xH_{2-x}Ti₃O₇, a transition-metal-doped protonated titanate (MnH-NTs) with maximal concentration of about $x \sim 0.18$. A subsequent heat treatment transforms it into Mn_yTi_{1-y}O₂ (Mn-NTs) with $y = x/(x + 3)$. The concentration y reaches a maximum of 5.6 at. %. Here we focus on the spatial distribution of Mn²⁺ in nanotubular titanates and on their magnetic response by using X-ray diffraction (XRD), electron spin

Received: October 22, 2012

Revised: December 12, 2012

Published: December 12, 2012

resonance spectroscopy (ESR), and SQUID techniques. We found two Mn^{2+} positions in the structure with cubic and strongly distorted octahedral local symmetries. ESR and SQUID measurements do not show a long-range magnetic order.

EXPERIMENTAL METHODS

In a typical synthesis, 1 g of titanium(IV) oxide nanopowder (99.7% anatase, Aldrich) is mixed with 30 mL of 10 M NaOH (97%, Aldrich) solution. The mixture is then transferred to a Teflon-lined stainless steel autoclave (Parr Instrument Co.) and heated to 130 °C and kept at this temperature for 72 h. After the treatment, the autoclave is cooled down to room temperature at a rate of 1 °C min^{-1} . The obtained $\text{Na}_2\text{Ti}_3\text{O}_7$ product is then filtered and washed several times with deionized water and neutralized up to $\text{pH} \approx 6.5$ with the appropriate amount of 0.1 M HCl solution (Merck). During this step, sodium exchange proceeds to the formation of $\text{H}_2\text{Ti}_3\text{O}_7$ nanotubes. The sample is finally washed with hot (80 °C) deionized water in order to remove any traces of NaCl. To dope $\text{H}_2\text{Ti}_3\text{O}_7$ nanotubes by Mn^{2+} , they are suspended in a $\text{Mn}(\text{NO}_3)_2 \cdot \text{H}_2\text{O}$ solution at 10 °C for 1 h. The suspension is subsequently filtered and washed with 500 mL of deionized water in order to remove the nonexchanged Mn^{2+} remaining in the solution. As a result, a solid $\text{Mn}_x\text{H}_{2-x}\text{Ti}_3\text{O}_7$ phase is obtained with x up to 0.18 (MnH-NTs). For Mn^{2+} -doped TiO_2 NTs, in the final step MnH-NTs undergo heat treatment at 400 °C in a reducing atmosphere (N_2/H_2) in order to prevent Mn^{2+} oxidation into higher oxidation states, and a single phase $\text{Mn}_y\text{Ti}_{1-y}\text{O}_2$ is obtained (Mn-NTs).

The manganese content was determined by energy-dispersive X-ray spectroscopy (EDX). XRD measurements were performed in $\Theta/2\Theta$ geometry on powder samples using $\text{Cu K}\alpha$ ($\lambda = 1.54056 \text{ \AA}$) radiation. The morphology of the samples was examined by low-/high-resolution transmission electron microscopy (TEM/HRTEM). Electron spin resonance (ESR) measurements of the nanotubes were carried out in an X-band spectrometer in the 5–300 K temperature range. SQUID measurements were performed on a S600 magnetometer following the zero-field-cooled/field-cooled (ZFC/FC) magnetization measurements.

RESULTS AND DISCUSSION

In Figure 1, the manganese ion concentration of MnH-NTs assuming complete ion exchange (nominal) versus the equilibrium manganese concentration (incorporated) after the ion exchange is depicted based on EDX measurements. The line in Figure 1 is a fit to an exponential saturation model $a(1 - e^{-bx})$. It yields $a = 18(1)$ at. % saturation concentration and $b = 0.052(6)$ characteristic exchange ratio. This doping level and Mn^{2+} exchange efficiency are seen as characteristics of the described synthesis method.

The kinetics of alkali metal ion intercalation between the layers of titanate nanotubes and nanofibers from aqueous suspension has been thoroughly studied by Bavykin et al.¹⁷ They found that the limiting stage of the process is likely to be the diffusion of ions inside the solid crystal which strongly depended on the length of the nanotubes. Here we focus on the elucidation of the state, local interaction, and spatial distribution of Mn^{2+} in nanotubular titanates and their derivatives after the steady-state concentration has been reached.

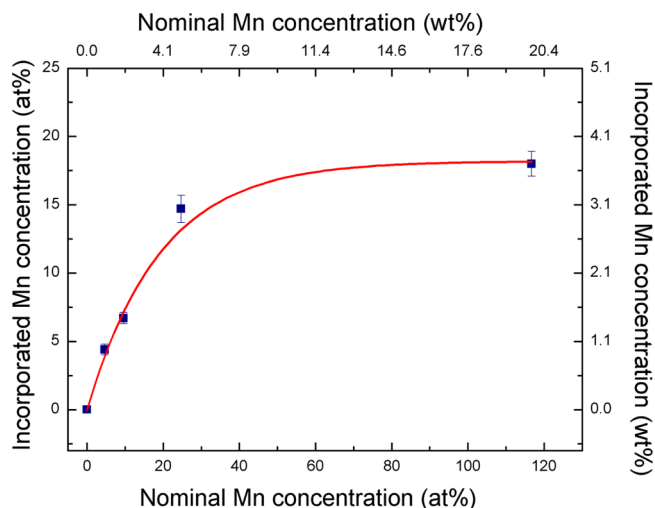


Figure 1. Nominal vs the incorporated Mn concentration ratio for the case of MnH-NTs. Line is a fit to an exponential saturation model $a(1 - e^{-bx})$ with $a = 18(1)$ at. % and $b = 0.052(6)$. The abbreviations contain the incorporated Mn concentration. The incorporated Mn concentration x of MnH-NT translates to $y = x/(x + 3)$ Mn concentration of Mn-NT upon heat treatment.

The powder XRD data measured on the MnH-NTs and Mn-NTs are given in Figure 2. The XRD pattern of the undoped,

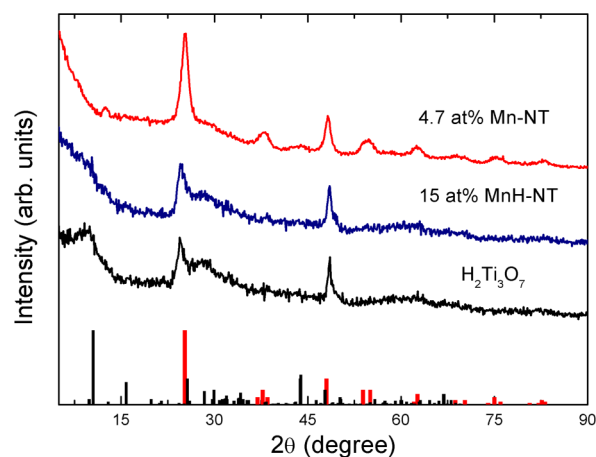


Figure 2. XRD spectra of undoped titanate ($\text{H}_2\text{Ti}_3\text{O}_7$) nanotubes, 15 at. % Mn-doped titanate nanotubes (15 at. % MnH-NT), and 4.7 at. % Mn-doped TiO_2 (4.7 at. % Mn-NT). The peak at $2\Theta = 13^\circ$ in 4.7 at. % Mn-NT originates from the sample holder.

protonated titanate nanotubes can be indexed as the monoclinic trititanate ($\text{H}_2\text{Ti}_3\text{O}_7$) phase.^{18,19} The characteristic reflection near $2\Theta = 10^\circ$ is correlated with the interlayer distance d_{200} in the wall of nanotubes. XRD profile of the 15 at. % MnH-NT compared to the undoped, protonated sample ($\text{H}_2\text{Ti}_3\text{O}_7$) shows the weakening of the peak near $2\Theta = 10^\circ$ upon the ion exchange. Similar weakening of this characteristic reflection was found by several authors.^{20–22} This could be related to the distortion of crystalline order within the layers due to the ion-exchange.

The heat treatment of MnH-NTs in reduced atmosphere resulted in the creation of Mn-NTs where TiO_2 exists in anatase phase TiO_2 (JCPDS 84_1285). No other peaks of minority phases as manganese titanate, metallic manganese, or its oxides have been observed.

In principle, in a solid the ion-exchange positions are spatially well-defined places. Therefore, we expect that the ionic exchange across the titanate nanoscrolls ensures that manganese ions do not create aggregates in the MnH-NT structure. Furthermore, the relatively low-temperature heat treatment process for making the Mn-NTs suppresses the diffusion and aggregation of Mn ions.

The TEM images of 4.7 at. % Mn-NT produced under heat treatment at 400 °C ascertain the prevailing tubular morphology of the doped TiO₂ material. Unlike the pristine trititanate nanotubes, the manganese-doped TiO₂ nanotubes are crystallized together near the contact point during the heat treatment, which results in highly aggregated nanotube secondary structure (Figure 3c,d). The effect of calcination

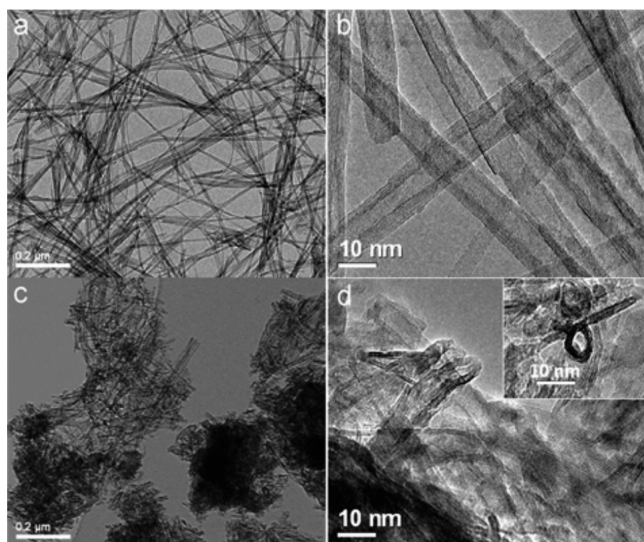


Figure 3. (a) TEM and (b) HRTEM image of pristine titanate nanotubes. (c) TEM and (d) HRTEM image of a 4.7 at. % Mn-NTs produced under heat treatment of MnH-NTs at 400 °C in a reducing atmosphere.

on the morphological evolution and phase transition of protonated titanate nanotubes has been studied by many researchers. It has been reported that upon calcination the gradual interlayer dehydration leads to a titanate-to-anatase crystal phase change accompanied by the transformation of the tubular shape into nanorods. Electron microscopic investigations revealed that the nanotubes still retain the tubular shape at 350–400 °C.²³

Neither XRD nor TEM measurements find segregated Mn-rich phases in the studied materials. Nevertheless, these techniques are limited to identifying about percent concentration minority phases. ESR, in contrast, is a dopant-specific spectroscopic technique that provides highly detailed microscopic information about the oxidation state and the local environment of the substituent paramagnetic ions in the crystal on ppm levels in principle. Furthermore, ESR is sensitive to the interactions between the paramagnetic ions. ESR spectroscopy has proven to be a very useful method for evaluating success in the synthesis of colloidal Mn²⁺-doped semiconductor nanocrystals.^{24,25} The theoretical background of ESR spectra of a large number of nanocrystals doped with Mn²⁺ has now been largely developed.^{26,27} The spin Hamiltonian that describes the spectra of Mn²⁺ is

$$H = H_Z + H_{CF} + H_{HF} + H_{e-e}$$

where first is the Zeeman term and second is the interaction with crystal electric fields. The third term describes the hyperfine coupling between the $S = 5/2$ electron spin and $I = 5/2$ nuclear spin of Mn²⁺. The last term is the interaction between neighboring Mn²⁺ ions.

Characteristic ESR spectra of MnH-NTs are given in Figure 4a. They confirm the presence of magnetically isolated Mn²⁺

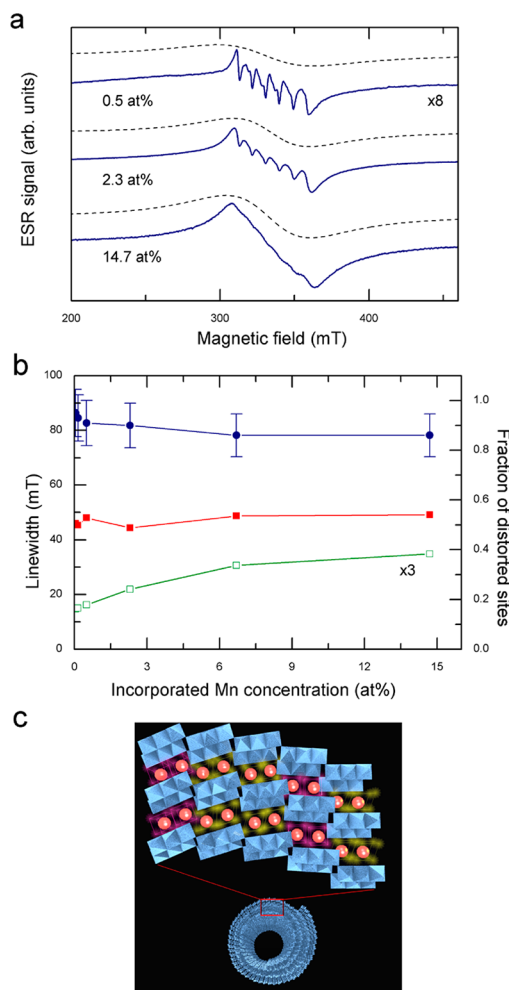


Figure 4. (a) Room-temperature ESR measurements on 0.5, 2.3, and 14.7 at. % MnH-NTs. Spectra are superposition of two ESR signal: a narrow sextet and a 48 mT broad line. Dashed lines are fits to the broad component. (b) ESR line width of individual hyperfine lines (□) and of the broad component (■) as a function of Mn concentration. Mn concentration dependence of the fraction of distorted Mn sites (●). (c) Schematic view of the tubular structure of MnH-NTs. Purple and yellow tetrahedrons represent slightly and strongly distorted Mn sites, respectively.

ions in the titanate nanotube structure. The spectra at all Mn²⁺ concentrations consist of two signals. One set of sextet lines dominates the spectra at low Mn²⁺ concentrations. In contrast, a 48 mT broad line is more pronounced at high Mn²⁺ concentrations.

The sextet signal is characteristic of a hyperfine splitting of ⁵⁵Mn with $g = 2.001(1)$ g -factor and $A_{iso} = 9.1$ mT hyperfine coupling constant. This spectrum corresponds to allowed ($\Delta m_I = 0$) and forbidden ($\Delta m_I = \pm 1$) hyperfine transitions between the Zeeman sublevels $m_s = \pm 1/2$. It is characteristic to Mn²⁺

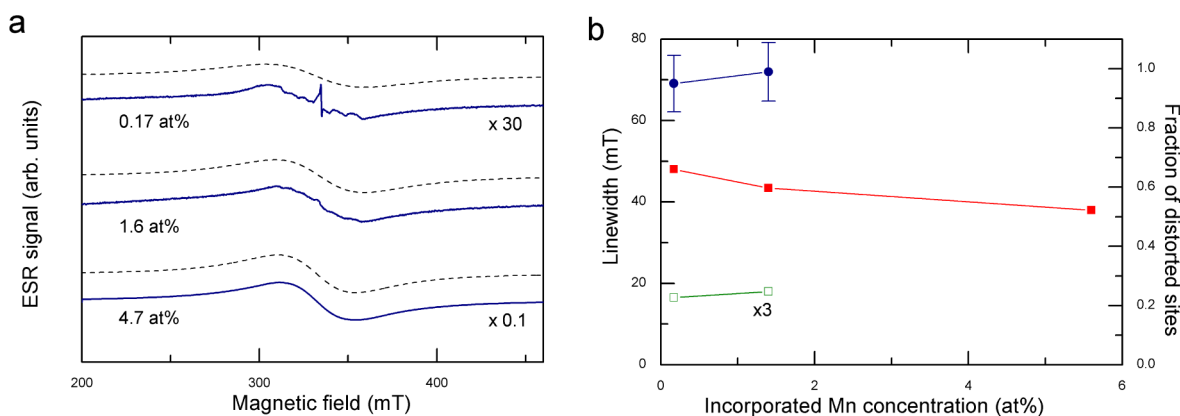


Figure 5. (a) Room-temperature ESR measurements on 0.17, 1.6, and on 4.7 at. % Mn-NTs. Spectra are superposition of three ESR signals: a narrow sextet, a 46 mT broad line (dashed lines), and the SETOV. (b) ESR line width of individual hyperfine lines (\square) and of the broad component (\blacksquare) as a function of Mn concentration. Mn concentration dependence of the fraction of distorted Mn sites (\bullet). At Mn concentration higher than 1.6 at. %, the strong broadening of the sextet lines impedes the sextet lines to be resolved. This explains the absence of data for the line width and fraction of distorted sites.

ions in octahedral crystal fields. However, since forbidden transitions are observable, Mn^{2+} ions do not occupy strictly cubic sites, as strictly cubic centers have zero probability of forbidden transitions, but the distortion relative to the cubic symmetry is small. The hyperfine coupling constant A_{iso} is essentially independent of the Mn^{2+} concentration. The width of the individual hyperfine lines increases by increasing the Mn^{2+} concentration (Figure 4b). Assuming only the dipole–dipole interaction between Mn^{2+} ions as an origin of the broadening following ref 28, the calculation yields $d_{\text{Mn-Mn}} = 1$ nm average distance at 15 at. %. This is a lower bound for the average Mn–Mn distance.

The broad Lorentzian signal around $g \approx 2$ (dashed line in Figure 4c) is superimposed to the narrow hyperfine sextet. The intensity of this broad line increases with the initial Mn^{2+} content; thus, it is intrinsic to ion-exchange. The 48 mT width of the broad line is essentially independent of Mn^{2+} concentration. It is about 5 times the $A_{\text{iso}} = 9.1$ mT, which is characteristic of Mn^{2+} ions located in strongly distorted octahedral sites. In powdered polycrystalline systems non-central transitions ($m_s \neq 1/2$) are always broadened and unresolved. This is due to the strong angular dependence of the lines and a parameter distribution in both hyperfine- and fine-coupling parameters. Dipolar interactions further broaden the lines. As previously determined, dipole–dipole interaction between Mn^{2+} ions broadens the sextuplet lines corresponding to the central $\Delta m_1 = 1$ transition. However, dipole–dipole interaction is not strong enough to smear out the hyperfine structure and thus produce the broad line. These findings are characteristic of Mn^{2+} -doped nanocrystals like Mn:CdS and Mn: TiO_2 .^{24,25}

The width of the broad line and the ratio $I_{\text{broad}}/(I_{\text{broad}} + I_{\text{hyperfine}}) = 0.85$ are found to be independent of the incorporated Mn^{2+} concentration for MnH-NTs (Figure 4c). Here, I_{broad} is the ESR intensity of the broad line and $I_{\text{hyperfine}}$ is the ESR intensity of the sextuplet. This also confirms that the broad Lorentzian curves in Figure 4 originate from distorted Mn^{2+} sites.

The question to be answered here is, what is the origin of the two different ion-exchange positions in the TiO_6 octahedra built host matrix? We speculate that the otherwise defectless layers of TiO_6 octahedra are not lined up in perfect registry due to the rolled up morphology of the trititanate nano-

tubes.^{29,30} Along this line, the 15% doping-independent fraction of high-symmetry Mn^{2+} positions are more likely a consequence of the incommensurate facing of titanium-centered octahedrons in neighboring walls due to the rolled-up structure of trititanate nanotubes (Figure 4b). Another possible explanation would be that structural imperfections (i.e., defects) have formed during the oriented crystal growth of the nanotubes, when these TiO_6 building bricks were arranged in space.²⁹

During heat treatment, MnH-NTs undergo dehydration to yield Mn-NTs. During the process, $\text{Mn}_x\text{H}_{2-x}\text{Ti}_3\text{O}_7$ is transformed into $\text{Mn}_y\text{Ti}_{1-y}\text{O}_2$. Mn/Ti stoichiometry remains constant, so that $y = x/(x + 3)$. For example, 5.6 at. % Mn-NTs originates from 18 at. % MnH-NTs.

Figure 5 depicts ESR on 0.17, 1.6, and 4.7 at. % Mn-NTs obtained after thermal treatment of the corresponding MnH-NTs. The spectra show the coexistence of a sextuplet and a broad Lorentzian line around $g \approx 2$ originating from Mn^{2+} ions similarly to Mn-NTs. Furthermore, a narrow symmetric line close to the free electron g -factor ($g = 2.003$) was also observed. This additional narrow line at $g = 2.003$ can be assigned to the single-electron-trapped oxygen vacancies (SETOV).^{18,31,32} The SETOV signal is induced by breaking of the Ti–OH bonds which follows the dehydration upon heat treatment. This is characteristic to all annealed titania nanotubes.^{18,24} The line width of the SETOV signal is $\Delta B_{\text{pp}} = 0.5$ mT in accordance with the literature.^{18,33} As already reported (in the 140–300 K temperature range),³³ ESR intensity of the SETOV satisfies the Curie law, confirming the presence of localized electrons. ESR measurements on the undoped TiO_2 (not shown) reveal the presence of the SETOV as well. At doping levels lower than 0.17 at. % (not shown), the SETOV signal dominates the spectra, but at all doping levels the SETOV concentration remains in the ppm level. At high Mn concentration, the broad Lorentzian curve overwhelms other signals.

The ESR intensity is essentially the same before and after the heat treatment of MnH-NTs. This indicates that Mn ions preserve their 2+ valence state during the heat treatment and Mn-NT formation. Furthermore, it is evidenced that the Mn^{2+} distribution remains homogeneous, and no Mn^{2+} clustering occurs during heat treatment. Similarly to MnH-NTs, the broad ESR signal stems from Mn^{2+} ions in distorted sites while the sextuplet at $g = 2.001$ proves that some Mn^{2+} ions occupy high

symmetry sites.^{24,25} However, due to the strong broadening of the sextet lines by increasing Mn concentration, the sextet lines were only resolved at low Mn concentrations. The hyperfine coupling constant is $A_{\text{iso}} = 12$ mT in the case of Mn-NT. The ratio of the two different Mn^{2+} lines is 5:95, which indicates that most of the Mn^{2+} ions occupy distorted sites (Figure 5b). The ratio increases relative to the MnH-NTs as a consequence of the different tube geometry.

ESR found the Mn-NT samples paramagnetic without a trace of magnetically ordered minority phase. However, X-band ESR is not always detectable on magnetically long-range ordered systems; thus, to further characterize the magnetic properties of Mn-NTs, SQUID measurements are required. Figure 6 depicts

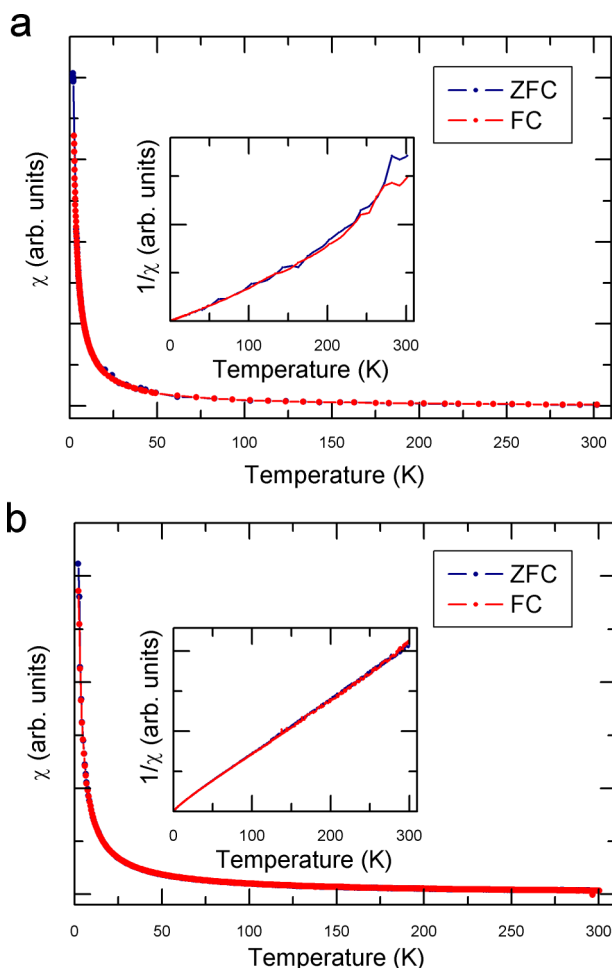


Figure 6. ZFC/FC SQUID measurements (a) for 0.17 at. % and (b) for 4.7 at. % Mn-NT. For FC, the applied field was 0.1 T. In the main panel the susceptibility (χ) is shown as a function of temperature. Inset presents $1/\chi$ as a function of temperature.

the ZFC/FC SQUID measurements for 0.17 and 4.7 at. % Mn-NT. The bulk susceptibility is of a Curie-like paramagnetic temperature dependence. This is further emphasized plotting $1/\chi$ as a function of temperature in the inset of Figure 6. The SQUID susceptibility is in agreement with the ESR intensity of the broad Lorentzian curves assigned to Mn^{2+} ions.

Earlier reports suggest that ferromagnetism in the fourth naturally occurring TiO_2 polymorph called $\text{TiO}_2(\text{B})$ is induced by the SETOV.³⁴ It has been proposed that the ferromagnetic coupling is induced through the F-center exchange mechanism.³⁵ Our measurements do not contradict these results. ESR

intensity, i.e., the spin susceptibility of the SETOV, is negligible compared to that of Mn^{2+} ions; thus, the paramagnetic behavior of 0.17 at. % Mn-NT is provoked by Mn^{2+} ions.

CONCLUSION

We have prepared homogeneously Mn^{2+} substituted $\text{H}_2\text{Ti}_3\text{O}_7$ (MnH-NTs) nanotubes by ion exchange. Two symmetrically different ion-exchange sites are identified by ESR spectroscopy. About 15% of the substituted Mn^{2+} ions occupy cubic sites, whereas 85% shows strongly distorted octahedral local symmetry. Low-temperature heat treatment transforms the titanate structure to $\text{Mn}_y\text{Ti}_{1-y}\text{O}_2$ nanotubes (Mn-NTs) while it maintains the homogeneity of the Mn^{2+} substitution. We report on the absence of ferromagnetic properties of single phase $\text{Mn}_y\text{Ti}_{1-y}\text{O}_2$ nanotubes which favors the scenario that ferromagnetism is of extrinsic origin in $\text{Mn}_y\text{Ti}_{1-y}\text{O}_2$.

The synthesis method presented here opens a novel pathway to synthesizing high-quality homogeneously diluted magnetic semiconducting TiO_2 nanotube powders. Besides the commonly used doping techniques employing vapor deposition or ion bombardment, the ion-exchange-based protocol could be used as a cost-effective, alternative way to obtain materials that cannot be prepared by heating mixtures of different precursors. Whereas these days vacuum deposition techniques are capable of controlling carrier concentrations moderately well, wet chemical methods to electronic doping are only now being developed and still suffer from many of the above-mentioned challenges. Here we have also demonstrated that ESR-active, ion-exchangeable cations can be seen as local probes to extract so far undetected information about the atomic level structure of nanotubular titanates and their derivatives.

The illustrated synthesis method could have long-term importance for the potential use of the ion-exchangeable titanate nanotube and nanowire powders in the DMS (diluted magnetic semiconductor) field.

AUTHOR INFORMATION

Corresponding Author

*E-mail arnaud.magrez@epfl.ch.

Notes

The authors declare no competing financial interest.

ACKNOWLEDGMENTS

This work was supported by the European project MULTIPLAT, by the Swiss National Science Foundation IZ73Z0_128037/1, and by the Swiss Contribution SH/7/2/20.

REFERENCES

- (1) Diebold, U. *Surf. Sci. Rep.* **2003**, *48*, 53–229.
- (2) O'Regan, B.; Grätzel, M. *Nature* **1991**, *353*, 737–740.
- (3) Garzella, C.; Comini, E.; Tempesti, E.; Frigeri, C.; Sberveglieri, G. *Sens. Actuators, B* **2000**, *68*, 189–196.
- (4) Fabregat-Santiago, F.; Randriamahazaka, H.; Zaban, A.; Garcia-Canadas, J.; Garcia-Belmonte, G.; Bisquert, J. *Phys. Chem. Chem. Phys.* **2006**, *8*, 1827–1833.
- (5) Forró, L.; Chauvet, O.; Emin, D.; Zuppiroli, L.; Berger, H.; Lévy, F. *J. Appl. Phys.* **1994**, *75*, 633–635.
- (6) Jacimovic, J.; Vaju, C.; Magrez, A.; Berger, H.; Forró, L.; Gaál, R.; Cerovski, V.; Zikic, R. *Europhys. Lett.* **2012**, *99*, 57005.
- (7) Tétreault, N.; Horváth, E.; Moehl, T.; Brillet, J.; Smajda, R.; Bungener, S.; Cai, N.; Wang, P.; Zakeeruddin, S. M.; Forró, L.; Magrez, A.; Grätzel, M. *ACS Nano* **2010**, *4*, 7644–7650.
- (8) Horváth, E.; Ribic, P. R.; Hashemi, F.; Forró, L.; Magrez, A. *J. Mater. Chem.* **2012**, *22*, 8778–8784.

- (9) Ogale, S. B. *Adv. Mater.* **2010**, *22*, 3125–3155.
- (10) Matsumoto, Y.; Murakami, M.; Shono, T.; Hasegawa, T.; Fukumura, T.; Kawasaki, M.; Ahmet, P.; Chikyow, T.; Koshihara, S.-y.; Koinuma, H. *Science* **2001**, *291*, 854–856.
- (11) Coey, J. M. D.; Venkatesan, M.; Fitzgerald, C. B. *Nat. Mater.* **2005**, *4*, 173–179.
- (12) Xu, L.; Xing, X.; Yang, M.; Li, X.; Wu, S.; Hu, P.; Lu, J.; Li, S. *Appl. Phys. A: Mater. Sci. Process.* **2010**, *98*, 417–421.
- (13) Sharma, S.; Chaudhary, S.; Kashyap, S. C.; Sharma, S. K. *J. Appl. Phys.* **2011**, *109*, 083905.
- (14) Tian, Z. M.; Yuan, S. L.; Wang, Y. Q.; He, J. H.; Yin, S. Y.; Liu, K. L.; Yuan, S. J.; Liu, L. *J. Phys. D: Appl. Phys.* **2008**, *41*, 055006.
- (15) Coey, J. *Curr. Opin. Solid State Mater. Sci.* **2006**, *10*, 83–92.
- (16) Nakajima, T.; Sheppard, L. R.; Prince, K. E.; Nowotny, J.; Ogawa, T. *Adv. Appl. Ceram.* **2007**, *106*, 82–88.
- (17) Bavykin, D. V.; Walsh, F. C. *J. Phys. Chem. C* **2007**, *111*, 14644–14651.
- (18) Cho, J.; Yun, W.; Lee, J.-K.; Lee, H.; So, W.; Moon, S.; Jia, Y.; Kulkarni, H.; Wu, Y. *Appl. Phys. A: Mater. Sci. Process.* **2007**, *88*, 751–755.
- (19) Kijima, T. *Inorganic and Metallic Nanotubular Materials: Recent Technologies and Applications*; Topics in Applied Physics; Springer: New York, 2010; pp 17–32.
- (20) Wang, X. W.; Gao, X. P.; Li, G. R.; Gao, L.; Yan, T. Y.; Zhu, H. *Y. Appl. Phys. Lett.* **2007**, *91*, 143102.
- (21) Morgado, E.; Marinkovic, B. A.; Jardim, P. M.; de Abreu, M. A.; da Graça C. Rocha, M.; Bargiela, P. *Mater. Chem. Phys.* **2011**, *126*, 118–127.
- (22) Sun, X.; Li, Y. *Chem.—Eur. J.* **2003**, *9*, 2229–2238.
- (23) Zhang, L.; Lin, H.; Wang, N.; Lin, C.; Li, J. *J. Alloys Compd.* **2007**, *431*, 230–235.
- (24) Counio, G.; Esnouf, S.; Gacoin, T.; Boilot, J. *J. Phys. Chem.* **1996**, *100*, 20021–20026.
- (25) Saponjic, Z. V.; Dimitrijevic, N. M.; Poluektov, O. G.; Chen, L. X.; Wasinger, E.; Welp, U.; Tiede, D. M.; Zuo, X.; Rajh, T. *J. Phys. Chem. B* **2006**, *110*, 25441–25450.
- (26) Allen, B. T. *J. Chem. Phys.* **1965**, *43*, 3820–3826.
- (27) Misra, S. K. *Physica B* **1994**, *203*, 193–200.
- (28) Van Vleck, J. H. *Phys. Rev.* **1948**, *74*, 1168–1183.
- (29) Kukovec, A.; Hodos, M.; Horváth, E.; Radnóczy, G.; Kónya, Z.; Kiricsi, I. *J. Phys. Chem. B* **2005**, *109*, 17781–17783.
- (30) Gateshki, M.; Chen, Q.; Peng, L.-M.; Chupas, P.; Petkov, V. Z. *Kristallogr.* **2007**, *222*, 612–616.
- (31) Serwicka, E.; Schlierkamp, M.; Schindler, R. *Z. Naturforsch., Sect. A: J. Phys. Sci.* **1981**, *36*, 226–232.
- (32) Serwicka, E. *Colloids Surf.* **1985**, *13*, 287–293.
- (33) Cho, J.; Seo, J.; Lee, J.-K.; Zhang, H.; Lamb, R. *Physica B* **2009**, *404*, 127–130.
- (34) Huang, C.; Liu, X.; Kong, L.; Lan, W.; Su, Q.; Wang, Y. *Appl. Phys. A: Mater. Sci. Process.* **2007**, *87*, 781–786.
- (35) Coey, J. M. D.; Douvalis, A. P.; Fitzgerald, C. B.; Venkatesan, M. *Appl. Phys. Lett.* **2004**, *84*, 1332.